**Proceedings of the Canadian Society for Mechanical Engineering International Congress**
**32nd Annual Conference of the Computational Fluid Dynamics Society of Canada**
**Canadian Society of Rheology Symposium**
**CSME-CFDSC-CSR 2025**
**May 25–28, 2025, Montréal, Québec, Canada**

# DRAG REDUCTION PERFORMANCE OF TRIANGULAR RIBLETS WITH VARIOUS INCLUDED ANGLES IMMERSED IN WATER-GLYCEROL MIXTURE

James Monk[1], William B. Gordon[1,2], O. Remus Tutunea-Fatan[1,2*], Evgueni V. Bordatchev[2,1**]
[1]Department of Mechanical and Material Engineering, Western University, London, Canada
[2]Automotive and Surface Transportation, National Research Council of Canada, University, London, Canada
*rtutunea@eng.uwo.ca, **evgueni.bordatchev@nrc-cnrc.gc.ca

***Abstract*** — This study presents the initial development of drag-reducing surfaces featuring streamwise triangular riblets at 30°, 60°, and 90°. It encompasses the design, microfabrication, and performance evaluation. Four acrylic cylindrical samples (drums), including one with a smooth surface, were fabricated by means of high-precision multi-axis single-point diamond cutting (SPDC) that yielded exceptional surface quality and form accuracy of <1 µm. The functional performance was assessed by means of a rheometer-based Taylor-Couette system that synchronously recorded frictional torque and angular position in the time domain at an angular speed of 230.6 rad/s. The 60° riblets demonstrated a 6.9% reduction in drag as measured through the decreased torque. Additional statistical metrics – such as standard deviation, amplitude-frequency characteristic, and probability density function - were used to evaluate the dynamics of riblet-fluid interactions. The findings of this study contribute to the further development of knowledge on drag-reducing functional surfaces with numerous potential applications in aerospace, automotive, marine, and energy sectors.

***Keywords-functional surface; triangular riblets; included angle; performance; analysis; Taylor-Couette system; drag reduction***

## I. INTRODUCTION

Functional surfaces are purposely engineered with geometric patterns that are meant to fulfill specific purposes, such as drag reduction or hydrophobicity. These surfaces have been a focus of active research for several decades. Among the possible microstructure shapes, streamwise grooves – commonly termed as riblets – are among the most extensively studied geometries used for drag-reduction purposes.

In general terms, drag force represents a dynamic link between a propellant/actuator (such as airflow) and system's response (such as wing deformations). The aerodynamics of airplanes, vessels, and vehicles involve two primary types of drag: pressure-induced drag, determined by the object's shape, and surface-induced drag, caused by the viscous friction between the airflow and surface microtopography. For aerodynamically shaped bodies, surface-induced drag can dominate pressure-induced drag by a significant margin (ranging from 5% to 90%) [1], since most friction losses occur at the flow-surface interface, particularly within the thin boundary layer that is in contact with the solid surface.

Surface topography disrupts flow, causing turbulence and three-dimensional variations in velocity, pressure, and shear stress. This leads to erratic convective patterns, unstable vortices, and increased skin resistance. As drag and turbulence intensify, the surface absorbs turbulent energy, converting it into viscous friction. Functional or structured surfaces offer broad industrial applications and strong research incentives. A key benefit, drag reduction, significantly impacts transportation by lowering fuel consumption and costs, as seen in shipping. In wind energy, microstructures like riblets on turbine blades reduce friction, enhancing efficiency. Due to the increasing desire to reduce emissions, energy costs, and to improve the performance of various modes of transportation, researchers have examined multiple types of textured surfaces that could significantly affect drag reduction (along with other quantitative and qualitative improvements). Within the broad diversity of possible microstructure geometries, streamwise structures were known to include scalloped riblets [2], blade riblets [3], sinusoidal riblets [4], trapezoidal riblets [5], and streamwise triangular riblets (also known as sawtooth riblets) [6].

Several theories have been proposed to explain the drag reduction mechanism, with a consensus that riblets achieve this by modifying fluid dynamics in similar ways. Specifically, they create a slower-moving fluid layer adjacent to the surface, reducing turbulent structures. Some researchers describe this phenomenon using the slip length – or virtual origin – which defines an imaginary flat surface within the riblet valley based on the velocity profile in the boundary layer [7]. Other theories suggest that riblets suppress spanwise velocity fluctuations in the riblet valley and above the peaks [8] or reduce streamwise

vortices near the surface [9]. Extensive research has explored different riblet geometries to optimize drag reduction. While passive approaches to drag reduction have seen limited breakthroughs, they remain valuable for industrial applications across various sectors.

The present study investigates the drag reducing performance of triangular riblets characterized by three different included angles when compared to a baseline smooth surface. For this purpose, experimental tests were performed by means of a rheometer-derived apparatus capable of developing Taylor-Couette flows in a water-glycerol mixture. During trials, the frictional torque was measured and recorded in time domain and several statistical metrics were used to evaluate drag reduction performance.

## II. Investigational Methodology

### A. Taylor-Couette Experimental Setup

The experimental setup relied on a Kinexus Pro+ rheometer (Malvern Instruments Ltd.) to evaluate the performance of textured cylindrical samples (drums) via Taylor-Couette flows (Fig 1). The high-precision spindle mounted on air-bearings represents one of the principal components of the rheometer. The spindle can be rotated with an angular velocity range from 10 nrad·s$^{-1}$ to 500 rad·s$^{-1}$. Other critical components of the experimental setup are the three sensors that can measure synchronously in time domain the following parameters: i) applied torque $Q(t)$ in a range from 10 nN·m to 200 mN·m with a resolution of 0.1 nN·m, ii) angular position $\alpha(t)$ with a resolution of under 10 nrad, and iii) normal force $N(t)$ in a range from 0.001 N to 20 N with a resolution of 0.5 mN. The rheometer supports shear rate and stress control modes, both used in experiments. The textured sample was fabricated from acrylic and was attached to the device spindle by means of a shaft with an M8x1 thread. The outer container was also made from transparent acrylic, was mounted on a rheometer base, and was accurately co-axially attached to the inner drum and spindle.

A Taylor-Couette (T-C) cell (Fig. 1b) was constructed of two coaxial components, namely an outer stationary cylindrical container and an inner textured cylindrical drum subjected to unidirectional rotational motion under the action of an electrical motor. The stationary container has a smooth inner surface (50.8 mm in diameter) whereas its outer diameter was 63.3 mm. Its total height, wall thickness, and base thickness were 100.2 mm, 6.35 mm, 12.7 mm, respectively. During the trials, each drum was precisely located 20 mm above bottom of the stationary container. The T-C cell was sealed off with a top lid penetrated by central hole for the spindle shaft that was also meant to prevent the overflow of the media/fluid (50-50% water-glycerol mixture) filling the gap between the stationary container and the sample to be tested. By accounting for all design parameters of the T-C cell and drum, the ratio of radii was $\eta = R_{drum}/R_{container} = 0.868$ whereas the height ratio was $\Gamma = L_{drum}/(R_{container} - R_{drum}) = 18.508$.

The sample drums were mounted to spindles, which directly locked into the rheometer. The drums are then lowered into the testing cylinder, which is then filled with water-glycerol solution as required to completely submerse the system. Upon confirmation that no air had been trapped in the system, the enclosure was sealed, and the system was ready for evaluation.

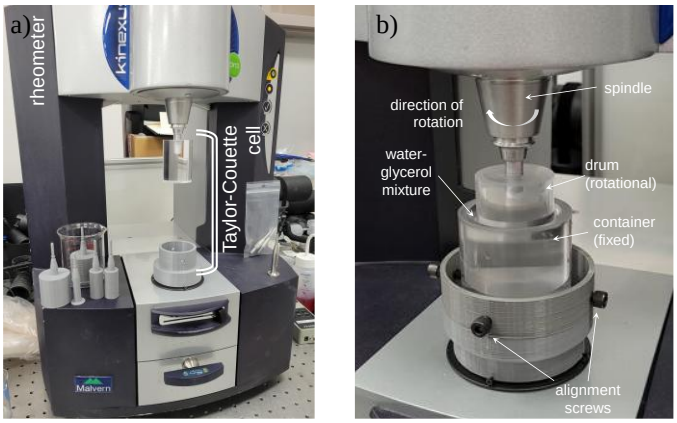


Figure 1. Experimental setup: a) rheometer and b) Taylor-Couette cell.

### B. Microfabrication of Functional Drums

A multi-axis micromachining system (MICROGANTRY nano5X, Kugler GmbH, Salem, Germany) was used to fabricate the functional drums by means of SPDC, a technology that was in the past to generate high-precision, high-quality functional parts [10], micro-optics [11], and structured surfaces [12]. The machining setup is depicted in Fig. 2a. As the photo shows, the vertically-oriented textured sample was mounted on an A/C tilt/swivel unit affixed to the Y-axis and a horizontally-mounted diamond cutting tool was attached to the X/Z motion table. The riblets were generated along the outer circumference of the workpiece by rotating the drum around A-axis while synchronously moving the cutting tool along Y and Z axes. For the purpose of this study, four cylindrical samples were fabricated: with a smooth surface, and with riblets characterized by 30°, 60°, and 90° included angles. Photos of smooth and with 30° included angles are shown in Fig. 2b.

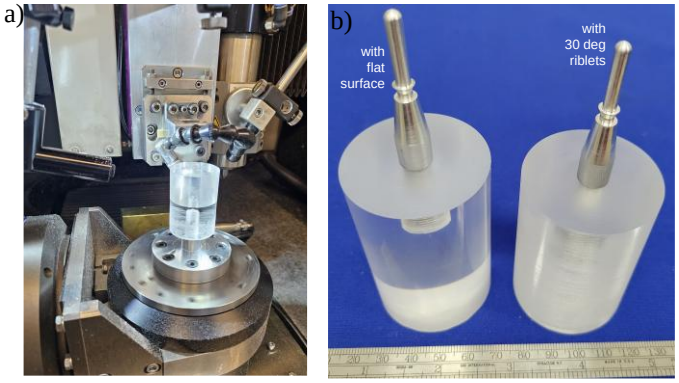


Figure 2. Microfabrication: a) machining setup and b) fabricated drums.

Surface topographies of drums with micromachined riblets were examined by means of a WYKO NT1100 (Veeco, Ltd., USA) an optical profilometer that offers an vertical resolution of 0.1 nm and an X-Y grid size of 192.98 nm. Since the textured cylindrical samples were fabricated at optical surface quality from a transparent acrylic, the optical profilometer was incapable to assess the complete surface topography of riblet

faces. More specifically, only the topography of surface areas that reflected the – light emitted by the internal source of the profilometer – could be evaluated. Commonly, these flat (or semi-flat) areas are located at the tip and bottom of the riblet. To exemplify this, the optical image of the cross-section and incompletely measured 3D topography with form parameters of the riblets with a 60° included angle are shown in Fig. 3. According to its design, the 60° riblets were to have a height of 50.0 µm and a spacing of 57.8 µm whereas their physical counterparts were manufactured with height of 50.7 µm and a spacing of 58.2 µm (form accuracy < 1.0 µm). Although the fabricated riblets had sharp but flat tips with small burs (of approximately 1-2 µm), the bottoms were also flat with a width of 2-3 µm. This is a consequence of the fact that the cutting tool has a flat tip to avoid tip breakage and extensive wear. The exceptional quality of the riblet faces is a critical parameter because has a high potential of confounding the drag reducing performance of the structured surface. Riblets were straight and had a good surface quality with minimum burr formation.

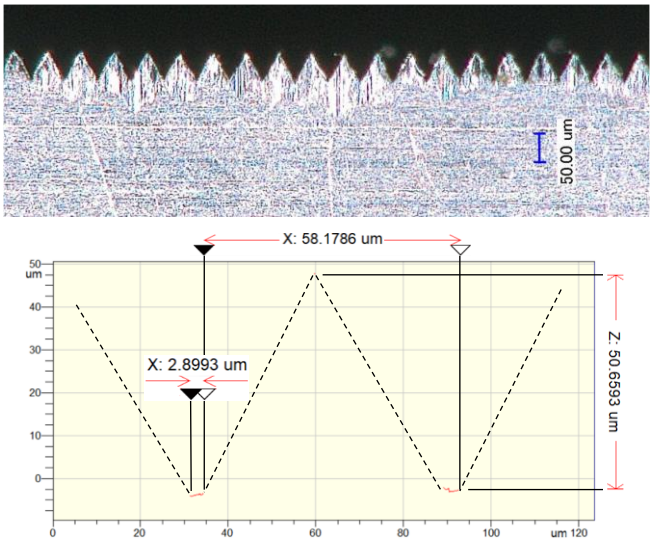


Figure 3. Microfabricated 60° riblets: a) cross section and b) dimensions.

### C. Experimental Data Analysis

During the experimental trials, the drum was attached to the spindle and rotated within a preset domain of angular speeds ranging from 8.3 rad/s to 264.8 rad/s with increments of 17.1 rad/s. Drum's rotation induced various types of inner volumetric shear flows and instabilities within the fluid and therefore generated a frictional torque in response to the dynamics of the fluid-surface interface. This frictional torque also corresponds to the drag developed within the T-C cell but with an additional contribution from the von Kármán flow present at the on the bottom flat face of the textured sample. During trials, data from the built-in sensors – time (s), angular position (deg), and torque (µN·m) – was recorded at an acquisition rate of 1 kHz by means of rSpace software (Malven Instruments Ltd.). Each drum underwent three experiments in a 50-50% water-glycerol mix, each being preceded by mass normalization before testing.

After the experiments were completed, the data acquired was stored in a text file for further analysis. The methodology used in this regard is presented in Fig. 4 and was implemented in MATLAB. The analysis involved a few consecutive steps:

- A specific angular speed was preselected for further analysis from the entire rage of speeds (Fig. 4a). After this, recorded torque data $Q(t)$ (Fig. 4b) was extracted. Of note, any sudden change in angular speed was always accompanied by a transient behavior. As such, the angular speed was allowed to increase after torque maintained a steady state for at least 10 seconds. Transient data was excluded from further analysis.
- A detailed view of the partial range of $Q(t)$ is shown in Fig. 4c, primarily for visual inspection purposes.
- In accordance with our prior studies involving water as a medium [13, 14], $Q(t)$ was separated into three components: mean torque $\bar{Q}$, kinematic component $\hat{Q}(t)$ characterized by amplitude $A$ and frequency of rotation $\omega$ (Fig. 4d), and dynamic component $\tilde{Q}(t)$ (Fig. 4e) induced by the hydrodynamic interactions at the flow-surface interface.
- Calculate mean and standard deviation (STD) values for $Q(t)$, $\hat{Q}(t)$, and $\tilde{Q}(t)$. Here, mean values asses a central measure of $Q(t)$ amplitudes whereas STD estimates the variability of $Q(t)$ amplitudes relative to the mean.
- Perform Fast Fourier Transformation (FFT) of $Q(t)$ and calculate an amplitude-frequency characteristic (A-FC) that shows a distribution of $Q(t)$ amplitudes in a frequency domain (Fig. 4f).
- Obtain an amplitude of A-FC at its dominant frequency ($\omega/2\pi$) that corresponds to a preselected angular speed . This value estimates an overall contribution of $\hat{Q}(t)$.
- The frequency range of A-FC within ]0, $\omega/2\pi$[ captures the dynamics of riblet-fluid interactions by $\tilde{Q}(t)$.
- Calculate a probability density function (PDF) of $\tilde{Q}(t)$, which assesses the state, ergodicity, stationarity, and chaoticity of the riblet-fluid interactions as a complex dynamic system (Fig. 4g).
- Collect all calculated statistical parameters (mean and standard deviation, STD) and functions (A-FC and PDF) for riblets with different included angles. All data was subsequently used to perform comparative analyses of their effect on functional performance (drag, shear stress, Taylor number, and other metrics associated with the hydrodynamics of the textured surface.

For evident reasons, the analysis of the extensive dataset collected during T-C trials (66,021 records per measured parameter with four parameters captured synchronously and in realtime) cannot constitute the subject of a single study. Therefore, a single angular speed (230.6 rad/s) was selected for a more detailed preliminary analysis to be used to further refine the advanced analysis methodology proposed herein.

## III. Analysis of the Effect of Included Angle

Past studies [15, 16] have proposed that four different flow types occur in T-C experiments: Couette flow, Taylor vortex

flow, wavy Taylor vortex flow, and turbulent flow. The degree of influence for each of these flow types depends on the Taylor number, radius ratio as well as height ratio. The centrifugal effect further complicates the dynamics of Taylor-Couette flows by inducing a pressure gradient in the radial direction. The frictional torque is influenced by no-slip boundary conditions between the container floor and the textured sample. Torque and normal force on the rotating drum are analyzed over time as functions of speed to assess riblet-fluid interactions. For brevity purposes, this study focuses solely on the frictional torque.

The functional performance of four cylindrical samples characterized by a smooth surface or textured with triangular riblets of 30°, 60°, and 90° included angles were experimentally assessed in a 50-50% water-glycerol mixture. Three measurement parameters (time, angular position, torque) were recorded for subsequent downstream analysis. As a first step, common statistical parameters such as mean and STD of actual $Q(t)$, kinematic component $\hat{Q}(t)$, and dynamic component $\tilde{Q}(t)$ were calculated (Table I). The analysis of $Q(t)$ shows that only $\bar{Q}_{60deg}$ is lower than $\bar{Q}_{smooth}$ (31.3 μN·m vs 33.6 μN·m) corresponding to a drag reduction of 6.9%. $\bar{Q}_{30deg}$ and $\bar{Q}_{90deg}$ values were lower than $\bar{Q}_{smooth}$ and therefore these riblet geometries are regarded as incapable of drag reduction under the tested conditions.

TABLE I. PARAMETERS OF FUNCTIONAL PERFORMANCE

| Parameters | | Riblet Height | | | |
|---|---|---|---|---|---|
| | | 00 deg | 30 deg | 60 deg | 90 deg |
| $Q(t)$ | Mean, μN·m | 33.6 | 33.7 | 31.3 | 34.1 |
| | Drag, % (+ increase, - decrease) | - | +0.3 | -6.9 | +1.5 |
| | STD, μN·m | 0.804 | 0.458 | 0.251 | 0.419 |
| | Max A-F amplitude, μN·m/Hz | 0.829 | 0.562 | 0.263 | 0.398 |
| $\hat{Q}(t)$ | Magnitude, μN·m | 2.213 | 1.284 | 0.616 | 0.946 |
| | STD, μN·m | 0.768 | 0.441 | 0.205 | 0.315 |
| $\tilde{Q}(t)$ | Magnitude, μN·m | 1.508 | 1.046 | 1.307 | 1.837 |
| | STD, μN·m | 0.219 | 0.136 | 0.145 | 0.273 |

It is also important to recognize how several statistical parameters (mean and STD) of $Q(t)$, $\hat{Q}(t)$, and $\tilde{Q}(t)$ characterize flow stability, variations within the flow as well as the effect of riblet-surface shear dynamics on frictional torque. For this purpose, these statistical metrics should be considered in conjunction with time and A-FC and PDF of $Q(t)$, $\hat{Q}(t)$, and $\tilde{Q}(t)$, all presented in Figs. 5-8. The STD of $Q(t)$ for all drums with riblets was less than STD of $Q_{smooth}(t)$. This can also be noticed by visually inspecting the time series of $Q(t)$ with and without riblets (Figs. 5a-8a and Figs. 5b-8b). By contrast, the digital signature of $Q_{smooth}(t)$ is more variable and with less amplitudes than that of textures samples. Parameters of $\hat{Q}(t)$ – magnitude, STD, and amplitude of the dominant frequency – exhibit a similar pattern of variation. These can be visualized in Figs. 5c-8c for magnitudes and STD of $\hat{Q}(t)$, in Figs. 5d-8d for magnitudes and STD of $\tilde{Q}(t)$, and in Figs. 5e-8e for A-FC of $Q(t)$. Contrasting to A-FC, PDF shows a distribution of $Q(t)$ amplitudes within the magnitude range. The STDs of $\tilde{Q}_{30deg}(t)$ and $\tilde{Q}_{60deg}(t)$, are less than STDs of $\tilde{Q}_{smooth}(t)$ and $\tilde{Q}_{90deg}(t)$. It can be visually confirmed that $\tilde{Q}_{smooth}(t)$ and $\tilde{Q}_{90deg}(t)$ have a more volatile appearance that clearly corresponds to a wide spread of PDFs of $\tilde{Q}_{30deg}(t)$ and $\tilde{Q}_{60deg}(t)$ depicted in Figs. 5f-8f.

## IV. SUMMARY AND CONCLUSIONS

The study presents preliminary findings on drag-reducing surface featuring streamwise triangular riblets with included angles of 30°, 60°, and 90°, and a height of 50 μm. Their drag reducing performances were compared to those of a smooth/untextured baseline. The four acrylic samples were precision-machined by means of SPDC, a process that yielded a superior dimensional precision and form accuracy (< 1 μm). The drag reduction performance of each sample was assessed by means of a rheometer-based Taylor-Couette system that is capable to synchronously record time, angular position, and torque. Statistical metrics such as standard deviation, amplitude-frequency characteristic, and probability density function, were used to evaluate the drag reduction phenomenon as well as the dynamics of riblet-fluid interactions. The following main conclusions can be drawn:

- A drag reduction of 6.9% was achieved for the textured cylindrical sample characterized by the 60° included angle. The drag reduction translated into a reduced mean value of the measured frictional torque.
- Riblet-mediated flow stability was detected through the statistical metrics of the measured torque. The 30° and 60° riblets showed reductions of magnitudes for torque kinematic and dynamic components.

These findings contribute to research on interfacial fluid dynamics and its applications in aerospace, automotive, marine, and energy sectors.


## ACKNOWLEDGMENT

The work presented in this study is the result of the collaboration between Western University (London, Ontario, Canada) and National Research Council of Canada.


## REFERENCES


[1] H.A. Abdulbari, H.D. Mahammed, and Z.B.Y. Hassan, "Bio-inspired passive drag reduction techniques: A review," ChemBioEng Reviews, 2015, 2(3), pp. 185–203.

[2] D.W. Bechert, M. Bruse, W. Hage, J.G.T. van der Hoeven, and G. Hoppe, "Experiments on drag-reducing surfaces and their optimization with adjustable geometry," J of Fluid Mechanics, 1997, 338, pp. 59–87.

[3] S. Martin and B. Bhushan, "Modeling and optimization of shark-inspired riblet geometries for low drag applications," Journal of Colloid and Interface Science, 2016, 474, pp. 206–215.

[4] M. Bonnivard, F.J. Suárez-Grau, and G. Tierra, "On the influence of wavy riblets on the slip behaviour of viscous fluids," Zeitschrift für angewandte Mathematik und Physik, 2016, 67(2), paper 27, 23 pp.

[5] D.W. Bechert and W. Hage, "Drag reduction with riblets in nature and engineering," WIT Transactions on State of the Art in Science and Engineering, 2006, 4, pp. 457–504.

[6] M.M. Zhang, Z.L. Zhang, and M. Zhao, "Investigation on the mechanism of drag modification over triangular riblets," Journal of Applied Fluid Mechanics, 2020, 13(4), pp. 1093–1106.

[7] G. Gómez-de-Segura, A. Sharma, and R. García-Mayoral, "Turbulent drag reduction using anisotropic permeable substrates," Flow, Turbulence and Combustion, 2018, 100(4), pp. 995–1014.

[8] R. Lueptow, "Taylor-Couette flow," Scholarpedia, 2009, 4(11), p. 6389.

[9] S.-J. Lee and S.-H. Lee, “Flow field analysis of a turbulent boundary layer over a riblet surface,” Exp in Fluids, 2001, 30(2), pp. 153–166.

[10] E.V. Bordatchev, M. Tauhiduzzaman, T. Kugler, A. Katz, and R. Bohr, “Demonstration of advanced capabilities of 5-axis micromilling: geometries with high-aspect ratio and/or optical surface quality,” Proc of the 8th Int’l Conf on Micro Manufacturing, 2013, pp. 357–362.

[11] B.W. Hamilton, S. Hussein, N. Milliken, O.R. Tutunea-Fatan, and E.V. Bordatchev, “Fabrication of right triangular prism retroreflectors through 3½½-axis ultraprecise single point inverted cutting,” Computer-Aided Design and Applications 2017, 14, pp. 693-703.

[12] B.W. Hamilton, O.R. Tutunea-Fatan, and E.V. Bordatchev, “Drag reduction by fish-scale inspired transverse asymmetric triangular riblets: Modelling, preliminary experimental analysis and potential for fouling control,” Biomimetics, 2023, 8, paper 324, 15 pp.

[13] E.V. Bordatchev, W.B. Gordon, O.R. Tutunea-Fatan, N. Song, and L. Li, "Drag reducing functional surface with 60 degree riblets," Proc. of AIAA SciTech Forum, 2025, paper 1676, 10 pp.

[14] W.B. Gordon, E.V. Bordatchev, O.R. Tutunea-Fatan, N. Song, and L. Li, “Preliminary Evaluation of Drag Reduction Performance for Functional Surfaces with 60-degree Riblets Subjected to Taylor-Couette Flows,” Proc. 5th Int’l Conf on Fluid Flow and Thermal Sc, 2024, paper 159, 8 pp.

[15] S. Grossmann, D. Lohse, and C. Sun, "High–Reynolds number Taylor-Couette turbulence," Annual Rev of Fluid Mech, 2016, 48(1), pp. 53-80.

[16] C.D. Andereck, S.S. Liu, and H.L. Swinney, “Flow regimes in a circular Couette system with independently rotating cylinders,” Journal of Fluid Mechanics, 1986, 164, pp. 155–183.

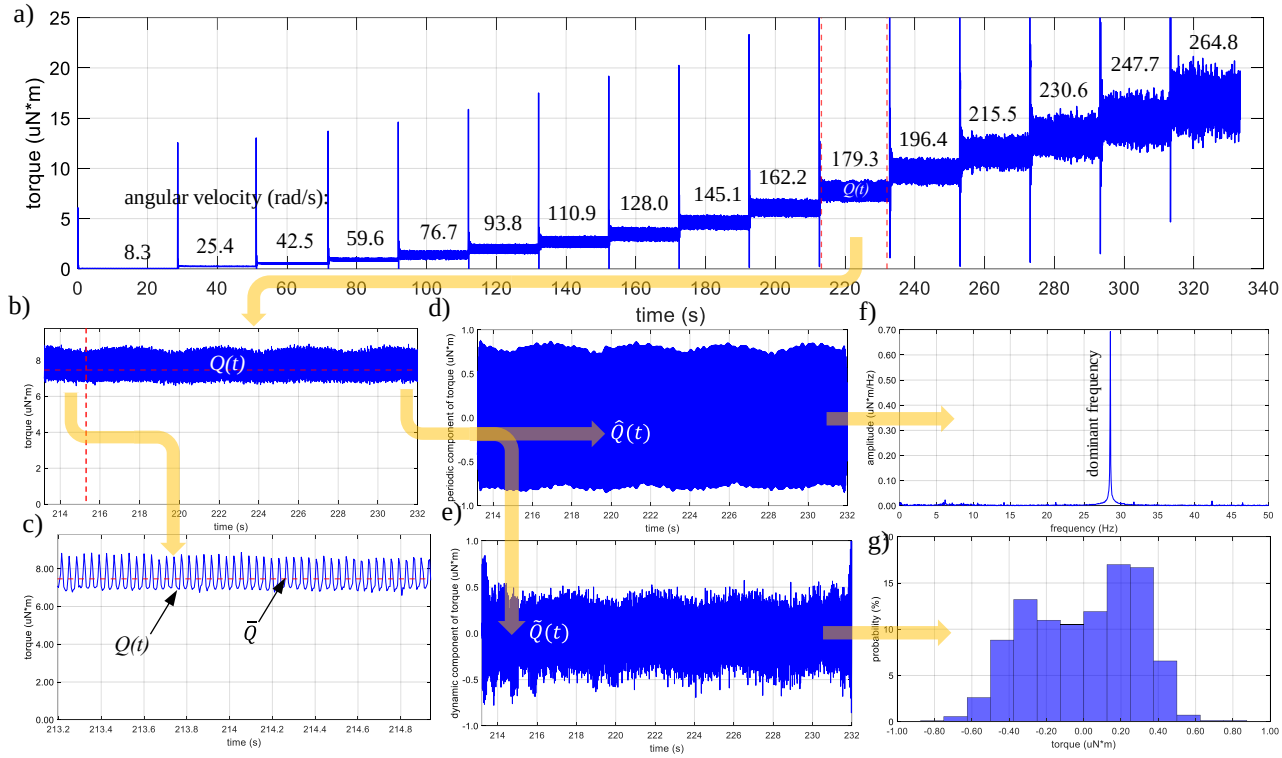


Figure 4. Experimental data analysis methodology: a) recorded torque for the whole range of speeds, b) selected torque for analysis, c) detailed view of torque variation, d) kinematic component, e) dynamic component, amplitude-frequency characteristic of measured torque, and probability density function of torque.

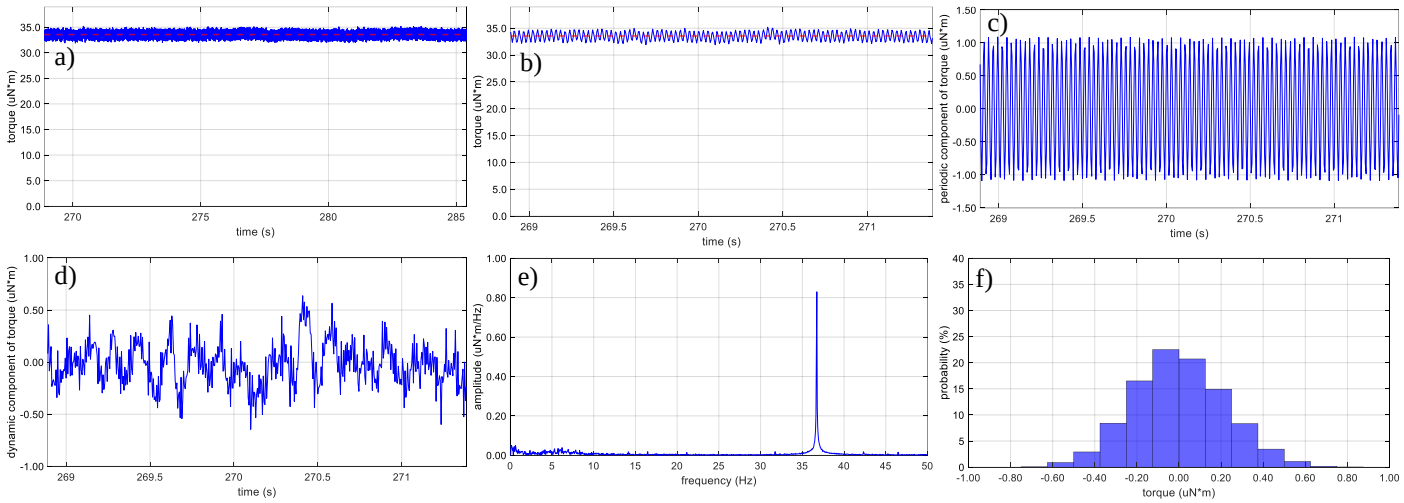


Figure 5. Functional performance of the drum with smooth surface at 230.6 rad/s angular speed: a) actual torque, b) detail of the actual torque variation, c) torque kinematic component, d) torque dynamic component, e) AFC of actual torque, and f) PDF of actual torque.

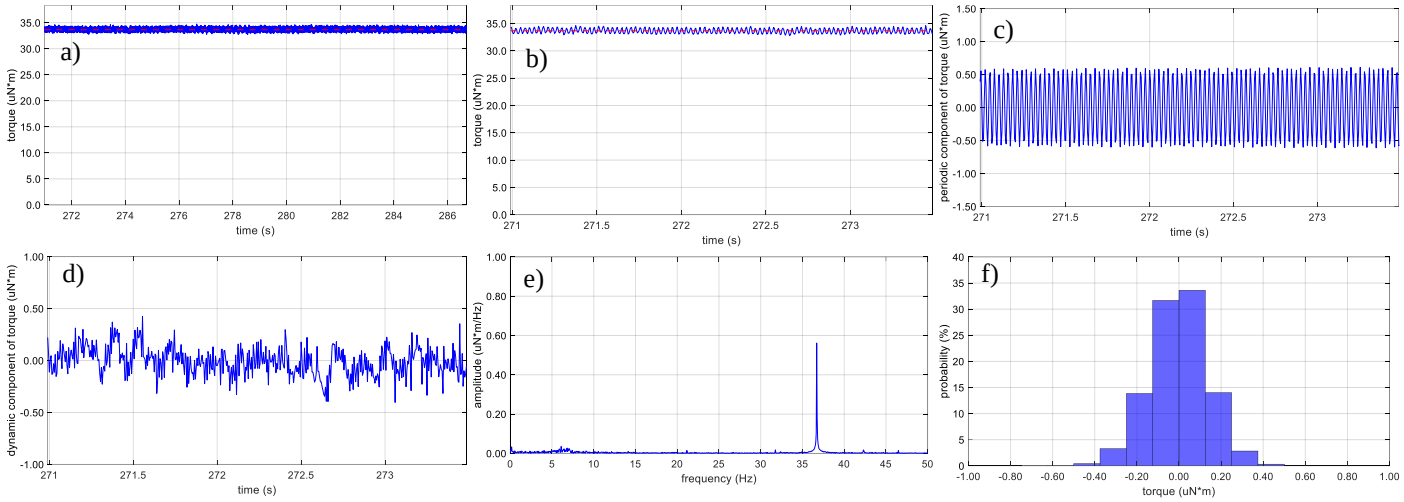


Figure 6. Functional performance of the drum with 30° riblets at 230.6 rad/s angular speed: a) actual torque, b) detail of the actual torque variation, c) torque kinematic component, d) torque dynamic component, e) AFC of actual torque, and f) PDF of actual torque.

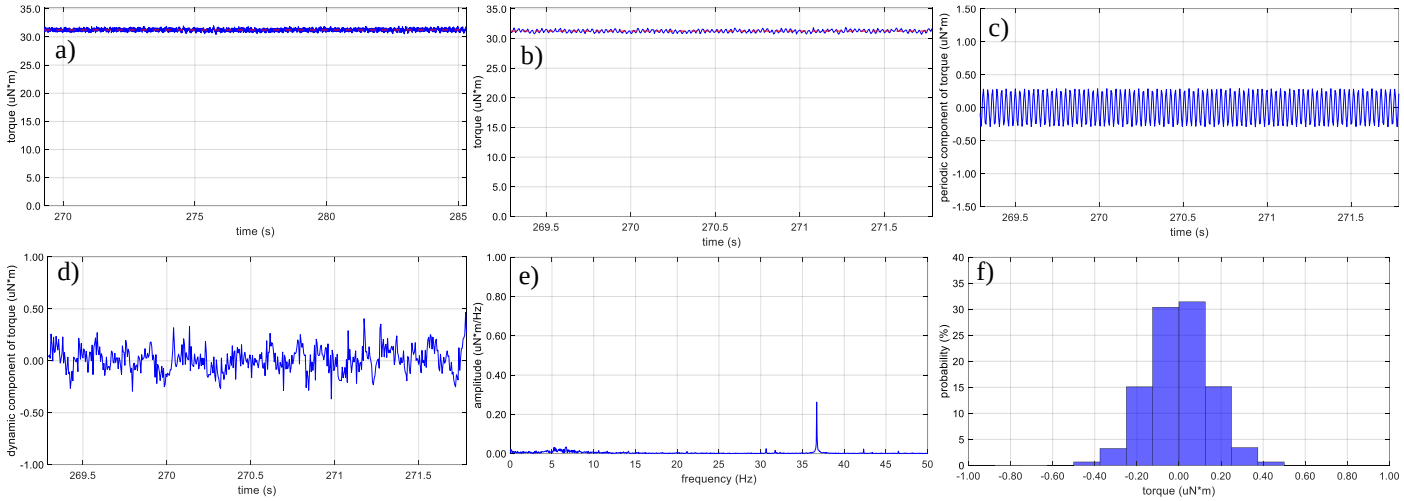


Figure 7. Functional performance of the drum with 60° riblets at 230.6 rad/s angular speed: a) actual torque, b) detail of the actual torque variation, c) torque kinematic component, d) torque dynamic component, e) AFC of actual torque, and f) PDF of actual torque.

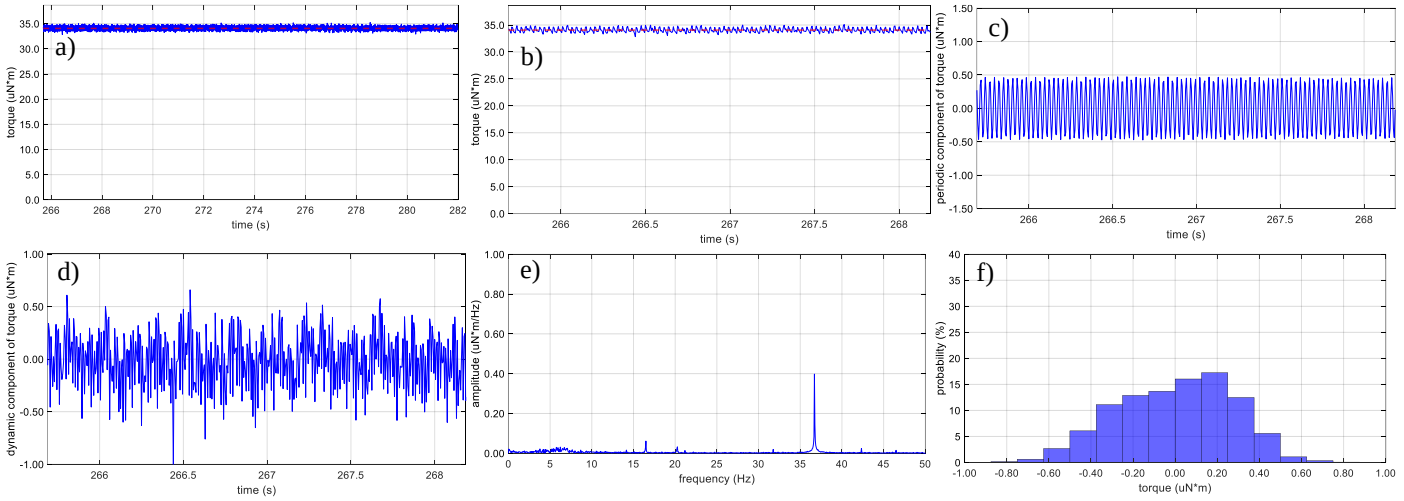


Figure 8. Functional performance of the drum with 90° riblets at 230.6 rad/s angular speed: a) actual torque, b) detail of the actual torque variation, c) torque kinematic component, d) torque dynamic component, e) AFC of actual torque, and f) PDF of actual torque.